Acid-Mediated Tumor Invasion: a Multidisciplinary Study

Robert A. Gatenby,[1,2] Edward T. Gawlinski,[4] Arthur F. Gmitro,[1,3]
Brant Kaylor,[3] and Robert J. Gillies[1]

Departments of [1]Radiology, [2]Applied Mathematics, and [3]Optical Sciences, University of Arizona, Tucson Arizona;
and [4]Department of Physics, Temple University, Philadelphia, Pennsylvania

Abstract

The acid-mediated tumor invasion hypothesis proposes altered glucose metabolism and increased glucose uptake, observed in the vast majority of clinical cancers by fluoro-deoxyglucose-positron emission tomography, are critical for development of the invasive phenotype. In this model, increased acid production due to altered glucose metabolism serves as a key intermediate by producing H⁺ flow along concentration gradients into adjacent normal tissue. This chronic exposure of peritumoral normal tissue to an acidic microenvironment produces toxicity by: (*a*) normal cell death caused by the collapse of the transmembrane H⁺ gradient inducing necrosis or apoptosis and (*b*) extracellular matrix degradation through the release of cathepsin B and other proteolytic enzymes. Tumor cells evolve resistance to acid-induced toxicity during carcinogenesis, allowing them to survive and proliferate in low pH microenvironments. This permits them to invade the damaged adjacent normal tissue despite the acid gradients. Here, we describe theoretical and empirical evidence for acid-mediated invasion. *In silico* simulations using mathematical models provide testable predictions concerning the morphology and cellular and extracellular dynamics at the tumor-host interface. *In vivo* experiments confirm the presence of peritumoral acid gradients as well as cellular toxicity and extracellular matrix degradation in the normal tissue exposed to the acidic microenvironment. The acid-mediated tumor invasion model provides a simple mechanism linking altered glucose metabolism with the ability of tumor cells to form invasive cancers. (Cancer Res 2006; 66(10): 5216-23)

Introduction

Fluorodeoxyglucose-positron emission tomography imaging has shown that the vast majority of human cancers exhibit significantly increased glucose flux compared with normal tissue (1, 2). This property seems to be a characteristic of invasive neoplasms and can be used to distinguish benign from malignant lung nodules (3). Increased glucose uptake is observed coincident with the transition from colon adenomas to invasive cancer (4) and from carcinoma *in situ* to invasive breast cancer (5). Furthermore, several studies have shown that increasing glucose uptake correlates with increasing tumor aggressiveness and progressively poorer prognosis (6–8).

The observed increase in glucose demand occurs on top of mitochondrial energy production and reflects an unregulated increase in the consumption and trapping of glucose beyond the cells' ability to oxidize pyruvate (9, 10). Some of the elevated glycolysis likely reflects adaptive changes to regions of intratumoral hypoxia that are caused by disordered vascularization with temporal and spatial variations in blood flow and oxygen delivery (11, 12). However, constitutive up-regulation of glycolysis is also observed even in the presence of adequate oxygen supplies (aerobic glycolysis): a phenomenon first noted by Warburg >80 years ago (13, 14).

We propose that this altered glucose metabolism and flux in malignant cells plays a critical role in cancer biology (15–17). Briefly, we hypothesize that the glycolytic phenotype first emerges as a survival mechanism in the regions of intermittent hypoxia that occur in premalignant lesions (17). These hypoxic regions are established as hyperplasia increases the spatial separation between intraluminal cells and their blood supply, which remains in the stroma separated from the tumor cells by an intact basement membrane. These dynamics result in cycles of hypoxia-normoxia (18). Adaptation to this unstable environment includes constitutive up-regulation of glycolysis, which remains elevated even in the presence of oxygen (in anticipation of the next anoxic episode). Elevated glycolysis also results in greater acid production, which is exacerbated by the increasing distance between cells and the acid sink provided by the blood vessels. Microenvironmental acidosis could lead to cellular necrosis and apoptosis (19, 20), adding additional selection forces that drive cancer cells to evolve phenotypes with increased resistance to acid-induced cellular toxicity (21, 22).

The net result of this evolutionary sequence is a cellular phenotype with a powerful adaptive advantage. These "aggressive" cancer cells alter their microenvironment by increased production of glycolytically derived acid. This is toxic to normal cell competitors but less harmful to the cancer cells themselves.

An extension of this concept is the acid-mediated tumor invasion hypothesis (15, 16, 23). We propose that invasive cancers continue to use the glycolytic phenotype to their advantage, thus explaining the persistence of aerobic glycolysis in clinically evident primary cancers and metastasis. The model includes the following components:

1. Increased glycolysis of cancers alters the microenvironment by substantially reducing intratumoral pH$_e$—a phenomenon observed experimentally (24–26).
2. H⁺ ions produced by the tumor diffuse along concentration gradients into adjacent normal tissues probably carried by a buffering species.
3. Acidification of the extracellular peritumoral environment is advantageous to the tumor because it:

   - induces normal cell death due to necrosis or caspase-mediated activation of p53-dependent apoptosis pathways (19, 20) and death of normal cells produces potential space into which the tumor cells may proliferate;

- extracellular acidosis also promotes angiogenesis through acid-induced release of vascular endothelial growth factor and interleukin-8 (27, 28);
- acidosis indirectly promotes extracellular matrix degradation by inducing adjacent normal cells (fibroblasts and macrophages) to release proteolytic enzymes such as cathepsin B (29), or increased lysosomal recycling (30);
- acidosis inhibits immune response to tumor antigens (31).

As discussed above, we propose that, during carcinogenesis, tumor cells evolve a phenotype which is adapted to environmental acidosis and is resistant to acid-mediated toxicity. This is observed experimentally as tumor cells survive and proliferate in pH_e significantly lower than that of normal cells (21, 22, 32), perhaps due to constitutive up-regulation of H^+ transporters or mutations in p53, caspase, or downstream effectors (22). *In vivo*, this phenotype confers a significant growth advantage as tumor cells proliferate in the acidic environment of the tumor-host interface allowing them to invade into the damaged normal tissue. Thus, the tumor edge can be envisioned as a traveling wave extending into normal tissue following a parallel traveling wave of increased microenvironmental acidity (16).

In the current report, this proposed mechanism of tumor invasion is tested in silico using mathematical models. We then present experimental observations of a peritumoral pH_e gradient extending into normal tissue and evidence of acid-induced toxicity in normal cells—both critical predictions of the hypothesis and of the mathematical models.

Materials and Methods

Mathematical Model

The tumor-host interface is a highly complex system dominated by nonlinear processes. The dynamics of this class of systems typically exhibit nonintuitive properties including extreme sensitivity to critical parameter values and rapid transitions between steady states with discontinuities and bifurcations. For this reason, we initially explored the hypothesis with mathematical models to test its feasibility in silico and gain some initial understanding of expected system dynamics (see Fig. 1). Below, we outline our general approach. Mathematically inclined readers are encouraged to review Appendix A for more details.

Building the model: spatial constraint of growth and migration. The acid-mediated tumor invasion hypothesis can be framed mathematically as a system of reaction-diffusion equations.

Using an approach previously described (16), we begin with spatial constraint: if N_1 and N_2 denote the cell densities (in cells/cm³) of the normal and tumor populations and assuming these populations only compete for available space, then their temporal evolution is governed by the following equations

$$\frac{\partial N_1}{\partial t} = r_1 N_1 \left(1 - \frac{N_1}{K_1} - \frac{N_2}{K_2} \right)$$

$$\frac{\partial N_2}{\partial t} = r_2 N_2 \left(1 - \frac{N_1}{K_1} - \frac{N_2}{K_2} \right)$$

(A)

where $r_{1,2}$ and $K_{1,2}$ are the growth rates (in 1/s) and spatial carrying capacities (in cells/cm³) of the respective populations. If it is also assumed that cells can migrate through space via a process akin to Fickian diffusion, in which the diffusion variables are themselves density-dependent (having a

maximum value in empty space and going to zero when cells are closely packed), then Eq. A becomes

$$\frac{\partial N_1}{\partial t} = r_1 N_1 \left(1 - \frac{N_1}{K_1} - \frac{N_2}{K_2} \right) + \nabla \cdot \left[D_{N_1} \left(1 - \frac{N_1}{K_1} - \frac{N_2}{K_2} \right) \nabla N_1 \right]$$

(B)

$$\frac{\partial N_2}{\partial t} = r_2 N_2 \left(1 - \frac{N_1}{K_1} - \frac{N_2}{K_2} \right) + \nabla \cdot \left[D_{N_2} \left(1 - \frac{N_1}{K_1} - \frac{N_2}{K_2} \right) \nabla N_2 \right]$$

where D_{N_1} and D_{N_2} (in cm²/s) are the "empty-space" diffusion constant of the normal and tumor cells, respectively. For simplicity, we will assume that these are approximately equal: $D_{N_1} \approx D_{N_2} = D_N$. The Lotka-Volterra terms ensure that the density-dependent diffusion parameters are always positive-definite $\in [0, D_N]$.

Building the model: effects of local pH. Next, we assume that each cell type has an optimal pH for survival and that if the local pH is perturbed from that optimal value, in either an acidic or an alkaline direction, the cells begin to die. We also assume that the death rate saturates at some maximum value when the environment is extremely acidic or alkaline. The simplest ad hoc functional form meeting these criteria is an "inverted Gaussian:"

$$f_{1,2}(H) = d_{1,2} \left[1 - \exp \left\{ - \left(\frac{H - H_{1,2}^{opt}}{2H_{1,2}^{width}} \right)^2 \right\} \right]$$

(C)

where H is the local concentration of H^+ ions (in mol/L), $d_{1,2}$ are the saturated death rates (in 1/s), $H_{1,2}^{opt}$ are the local H^+ ion concentrations (in mol/L) corresponding to the optimal pH's, and $H_{1,2}^{width}$ are the half-widths of the inverted Gaussian (in mol/L). Including the death rates Eq. D into Eq. B, we finally get

$$\frac{\partial N_1}{\partial t} = r_1 N_1 \left(1 - \frac{N_1}{K_1} - \frac{N_2}{K_2} \right) - f_1(H)N_1 + D_N \nabla \cdot \left[\left(1 - \frac{N_1}{K_1} - \frac{N_2}{K_2} \right) \nabla N_1 \right]$$

(D)

$$\frac{\partial N_2}{\partial t} = r_2 N_2 \left(1 - \frac{N_1}{K_1} - \frac{N_2}{K_2} \right) - f_2(H)N_2 + D_N \nabla \cdot \left[\left(1 - \frac{N_1}{K_1} - \frac{N_2}{K_2} \right) \nabla N_2 \right]$$
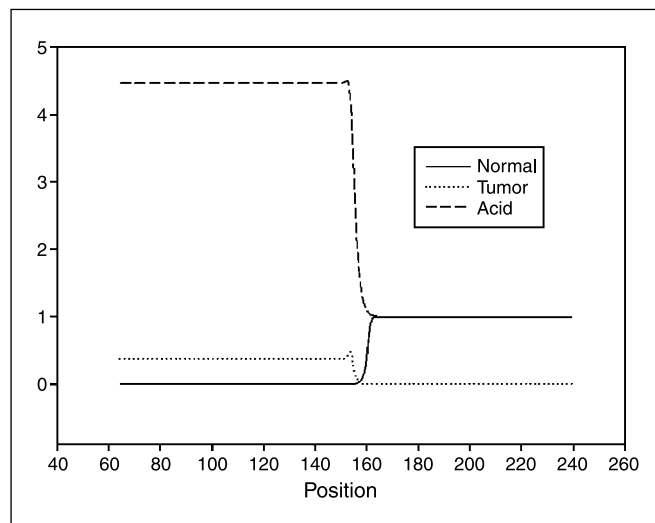

Figure 1. The dynamics of the tumor-host interface predicted by simulations from the mathematical model. The tumor edge is a traveling wave moving left to right preceded by a wave of acid extending into the peritumoral normal tissue. This results in a complementary traveling wave of receding normal tissue moving left to right as a result of acid-induced toxicity.

Building the model: acid production and uptake. We assume that H^+ ions are produced at a rate proportional to the local concentration of tumor and removed by the combined effects of buffering and vascular evacuation, both of which are proportional to microvessel areal density. Thus,

$$\frac{\partial H}{\partial t} = r_3 N_2 - d_3(H - H_0) + D_3 \nabla^2 H \qquad (E)$$

where H is the H^+ ion concentration (in mol/cm^3), r_3 is the H^+ ion production rate (in mol/(cell s)), d_3 is the H^+ ion uptake rate (in 1/s), H_0 is the H^+ ion concentration in serum, and D_3 is the H^+ ion diffusion constant (cm^2/s).

Experimental Methods

Tumors. *In vivo* experiments were done using two cell lines: MCF7/s and PC3N/enhanced green fluorescent protein (eGFP). The former is a human breast cancer that grows relatively slowly *in vivo*, whereas the latter is a rapidly growing human prostate cancer. Prior *in vitro* studies had measured proliferation rates, acid production, acid tolerance, and acid diffusion rates in both cell populations. Both lines were transfected with GFP to allow accurate tumor size and edge detection *in vivo* using fluorescent microscopy (Fig. 2).

Experiments were done in severe combined immunodeficiency (SCID) mice (6-8 weeks of age; 25-30 g) bred and housed in a defined flora animal colony. A dorsal skin fold chamber (Fig. 2) was surgically implanted under anesthesia (75 mg of ketamine and 25 mg of xylazine per kg s.c.), as described previously (33). After a 2-day recovery period, the coverslip in the chamber was gently lifted and a slurry of 2.5 to 3×10^6 tumor cells were placed on the exposed surface near the center of the chamber. Tumor growth was monitored using fluorescent microscopy approximately every 2 days. pH_e experiments were done when tumors reached a diameter of ~3.0 mm. Subsequent pH_e imaging was determined by tumor growth as assessed by fluorescent microscopy. The PC3N/eGFP typically began to grow immediately following placement so that images were generally obtained every 2 to 3 days. The MCF7/s tumors exhibited a long lag phase in which there was initially no growth so that pH_e maps were typically obtained every 5 to 7 days. Imaging continued until the tumor occupied >50% of the chamber area. In some cases, the tumors did not grow and imaging was discontinued once tumor regression was observed.

pH_e measurements. Extracellular pH was measured using SNARF-1 (Molecular Probes, Eugene, OR), which exhibits a spectral shift in fluorescence emission with change of pH_e and has been well described in the literature (34). Spatial distribution of pH_e in the tumor and adjacent normal tissue was obtained using ratiometric imaging with two sets of data measuring the intensity values collected in two different spectral emission regions and converting the ratios to a pH image using calibration data.

Images were obtained with a Nikon Eclipse E-600 microscope with a Nikon C-1 confocal microscope attachment in epi-illumination mode. Light sources on this instrument include two helium:neon lasers at 543 and 632 nm, and an argon laser operating at 488 nm. Fluorescence detection was obtained through three photomultiplier tubes (PMT) set to detect fluorescence emission using a 515/30 nm filter, a 595/50 nm filter and a 640 nm long pass filter, respectively. Channel 1 was used to view the emission from GFP; channels 2 and 3 were used to capture the two spectral signals from the SNARF fluorescence emission. The 543 He:Ne laser was used to excite the SNARF fluorescence and the argon laser was used to excite the GFP. The signals from the PMTs are read by Nikon's EZ-C1 software and displayed as an image. The software is capable of simultaneously collecting 12-bit images from each PMT channel.

During the imaging procedure, the mice were anaesthetized with ketamine HCl (100 mg/mL), xylazine (20 mg/mL), and acepromazine maleate (10 mg/mL) (Phoenix Pharmaceuticals, Inc., Belmont, CA). The anaesthetized mouse was placed in a Plexiglas holder and the window chamber attached rigidly to the microscope stage to prevent movement. Initially, a GFP image was captured with both the $2\times$ and $1\times$ objective to accurately determine the tumor borders. Fluorescent images were then obtained using both the $2\times$ and $1\times$ objectives and the 543 He:Ne laser to
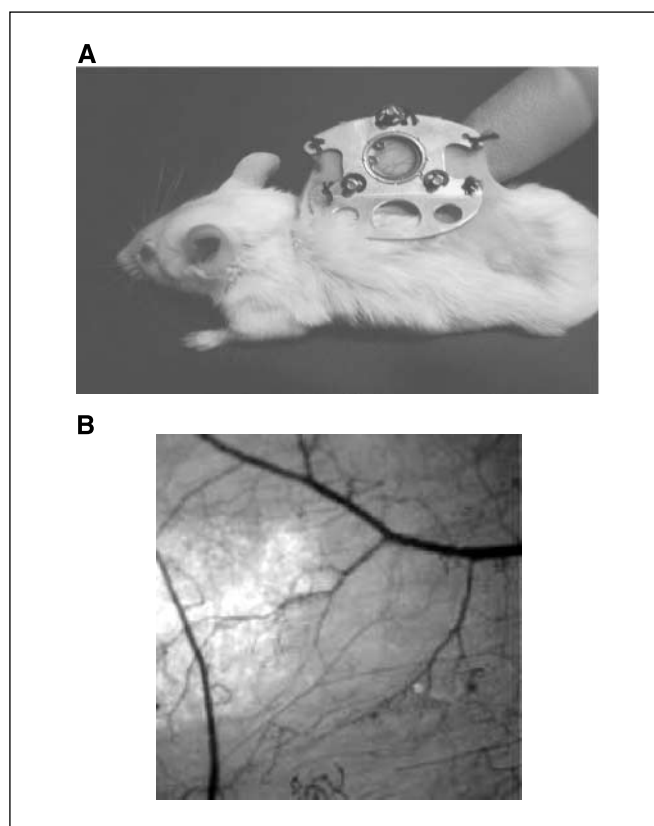

Figure 2. *A*, the dorsal window chamber in a SCID mouse. *B*, a fluorescent micrograph (original magnification, $\times$2) showing GFP-transfected tumor cells allowing definite identification of the site of the tumor-host interface.

obtain background fluorescence to be subtracted from subsequent images. Two hundred microliters of the 1 mmol/L SNARF solution in saline was injected via the tail vein catheter. Images were then collected using the green He:Ne laser with both objectives at 15, 30, and 40 minutes after injection.

The autofluorescence background image taken before injection of the dye was subtracted on a pixel-by-pixel basis from the SNARF fluorescence images to obtain only the SNARF fluorescent signal for each channel. The background-subtracted images were smoothed (i.e., convolved with a 2×2 rect function) before calculating the ratio image. This smoothing has the effect of reducing high-frequency noise, but spatial resolution is also reduced. The images from each channel were smoothed before the ratio was calculated. The intensity ratios were converted to pH_e images following calibration for SNARF-1 in buffered solutions of varying pH as measured by a pH electrode in a 96-well plate. Three sets of calibration data were taken from the same solution on consecutive days.

Analysis of pH_e gradients at the tumor-tissue interface was accomplished via the following procedure. The centroid and peripheral edge of the tumor were determined from the high-contrast GFP image. The pH_e image was then segmented into eight directions defined as angular segments of 45 degrees from the centroid of the tumor. Within each angular segment, a binary image of tumor versus nontumor was created based on the tumor edge. Binary dilation and contraction operations were employed to grow or contract the edge of the tumor by selected distances in steps equivalent to a distance of five pixels. These dilations and contractions defined tissue regions extending either out or in, respectively, from the tumor edge. The pH_e values were then averaged in these regions to yield the average pH_e relative to distance from the edge. The values of pH_e were then plotted as a function of distance from the edge for each of the eight angular segments. In some cases, angular segments were discarded if they did not correspond to valid data (e.g., the tumor was at the edge of the field of view in the window chamber so that for certain angular segments there was no

"normal" tissue outside the tumor boundary). The pH$_e$ data can be used to estimate the flow of H$^+$ ions at the tumor edge. This is done after binning the 512 × 512 image to 64 × 64. The gradient at the centroid of four adjacent points is calculated. The gradient array is displayed as arrows, a built-in capability of the IDL program. The arrows are then overlaid on the preexisting ratio image.

Microscopic evaluation. After completion of the sequence of pH$_e$ imaging experiments, the xenograft tissues were harvested, fixed in 10% neutral buffered formalin for 24 hours, processed and embedded in paraffin. Routine H&E and periodic acid Schiff (PAS) stains were done on 3 μm sections of tissue. Cleaved caspase-3 was detected by immunohistochemistry using the Ventana Medical Systems (Tucson, AZ) Discovery XT automated platform. Rabbit polyclonal anticleaved caspase-3 (Cell Signaling Technology, Danvers, MA) was incubated for 2 hours at 37°C at a dilution of 1:200, and detected with a biotinylated streptavidin-horseradish peroxidase and 3,3′-diaminobenzidine detection system.

Results

Model results. Numerical simulations from the models can then be done using parameter estimates based on experimentally determined proliferation rates, acid production, and acid-induced toxicity in the cell lines used in subsequent experiments. This allows the models to produce detailed predictions about cellular and microenvironmental dynamics at the tumor-host interface. The details of this analysis are included in Appendix A.

In Fig. 1, numerical solutions show that the interface, at any given time, represents a snapshot of a traveling wave as tumor cells advance and normal cells recede. The tumor wave is preceded by a gradient of excess H$^+$ extending into adjacent normal tissue. Within the region of peritumoral acidosis, the models predict a loss of normal tissue due to acid-induced cellular toxicity and extracellular matrix breakdown. These results support the feasibility of the acid-mediated invasion model. The models showed that we should be able to experimentally detect a peritumoral acid gradient. Using parameter estimates available in the literature, it seemed likely that observation of the gradient and associated toxicity would require a spatial resolution in the range of ≤50 μm. This limited the appropriate experimental approach to fluorescent microscopy rather than, for example, magnetic resonance imaging or positron emission tomography.

Experimental results. The calibration studies showed that pH resolution of the fluorescent images was, on average, 0.042 pH units and none of the pH values varied by >0.02 over 3 days.

In vivo measurements showed that all of the tumors exhibited a significantly acidic pH$_e$ when compared with normal tissue. Average pH values across the entire regions of interest in growing tumors were 6.91 ± 0.14 for MCF-7 tumors (n = 4) and 6.83 ± 0.21 for the PC3N tumors (n = 10). These data compare favorably to pH$_e$ values measured using other approaches. For example, although the average pH$_e$ decreased with tumor size, the pH$_e$ of small (3-500 mm^3) MCF-7 tumors was 6.99 ± 0.11 as measured with ^{31}P MRS (35).

All of the PC3N/eGFP tumors showed a gradient of acidification extending from the tumor edge into the adjacent tumor over a typical distance of 100 to 400 μm on the first postimplantation images. All but one of these tumors continued to exhibit a significant gradient during subsequent imaging. As shown in Fig. 3, the gradient in the initial images was typically quite uniform but less so on later imaging. This spatial heterogeneity seemed to be the result of angiogenesis because the tumor was relatively avascular on the first images, but showed significant vascular growth in later studies. The expected flow of H$^+$ from the tumor edge into the

peritumoral normal tissue as a result of the gradients is shown in Fig. 4.

One PC3N/eGFP tumor failed to maintain a pH$_e$ gradient into adjacent normal tissue and also exhibited no growth before finally regressing.

A peritumoral pH$_e$ gradient was not observed initially in the MCF7/s tumors which also did not exhibit any significant growth for ~21 days following implantation. However, following this lag phase, rapid growth was observed simultaneously with onset of complete acidification of the chamber. Because all of the normal tissue in the chamber became acidic, the depth of the peritumoral gradient could not be determined but was clearly larger than that of the prostate cell line.

Three of the MCF7/s tumors, despite successful initial implantation, failed to grow and eventually involuted. In all cases, the initially acidic intratumoral pH$_e$ returned to normal values as tumor growth failed.

The relatively shallow peritumoral pH$_e$ gradient observed in the PC3N/eGFP tumors allowed the local effects on the normal tissue within the acidic gradient to be assessed. Following the *in vivo*
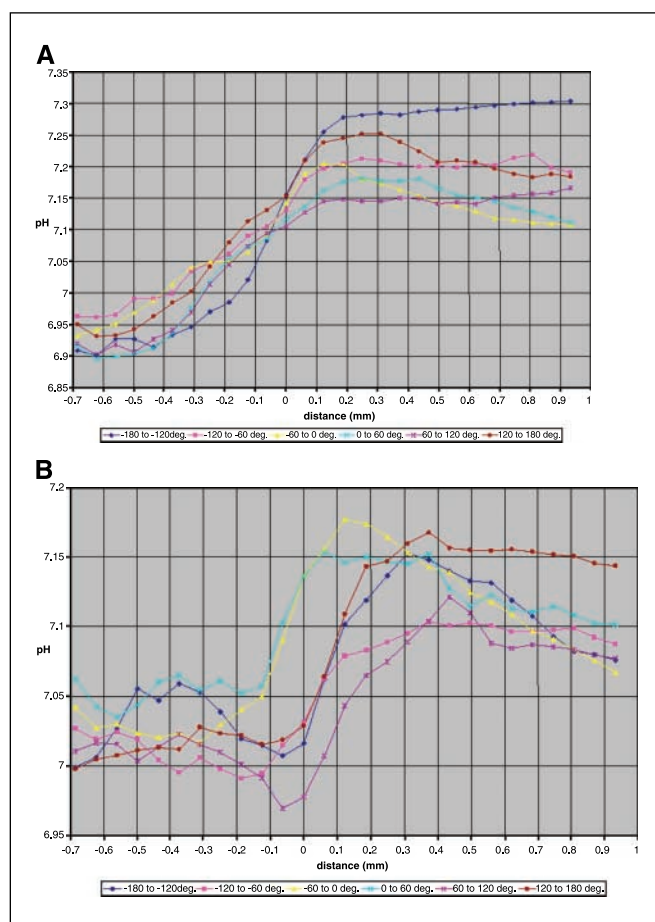

Figure 3. pH$_e$ gradients at the PC3N/eGFP tumor-host interface along radians drawn from the tumor center. The tumor-host interface is designated as the 0 point on the *x*-axis. All of the experiments showed a peritumoral acid gradient that was qualitatively and quantitatively similar to the results from the mathematical model in Fig. 1. Values obtained 2 days following placement of the tumor slurry (*A*). The relatively avascular tumor shows a fairly uniform pH$_e$ distribution and gradient. Values obtained 4 days later (*B*). During that time, significant tumor growth was observed. Note that the pH$_e$ distribution is less uniform, presumably representing increasing microenvironmental heterogeneity due to variations in tumor vascular distribution and flow.
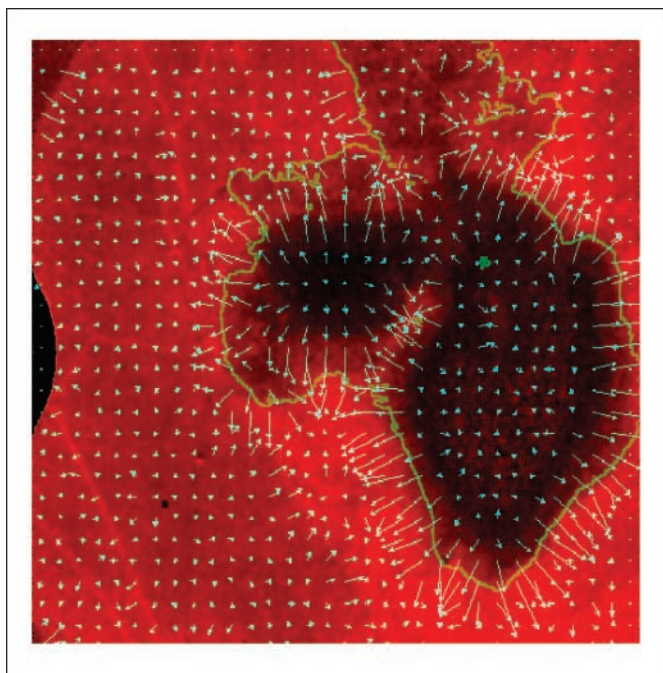
Figure 4. A map of peritumoral H^+ flow using vectors generated from the pH_e distribution around PC3N/eGFP. The tumor is the darker region (*left*) and the tumor-host interface is drawn based on the GFP image. *Arrows,* direction of H^+ flow and the length of each arrow is dependent on the slope of the gradient (the steeper the gradient, the longer the arrow). Note the general flow of H^+ from the tumor core to its periphery, and from there, into the normal tissue, although there is significant heterogeneity.

experiments, the mice were sacrificed and the tissue in the chamber was removed and fixed. As shown in Fig. 5, caspase stains from these samples showed evidence of apoptosis in multiple cells adjacent to the tumor edge in the acidic regions shown on FRIM images. H&E stains also show evidence of toxicity in skeletal muscle cells immediately adjacent to the tumor edge but not those more distant. In Fig. 6, PAS stains showed evidence of considerable degradation in the extracellular matrix immediately adjacent to the tumor edge.

Discussion

The acid-mediated tumor invasion hypothesis proposes that increased glycolysis, a phenotypic trait almost invariably observed in human cancers, confers a selective growth advantage on transformed cells because it allows them to create an environment toxic to competitors but relatively harmless to themselves. Specifically, this model hypothesizes that cancer cells use inefficient glycolytic pathways even in the presence of oxygen because it results in increased acid production, and a decrease in microenvironmental pH_e. Through an evolutionary sequence during carcinogenesis, tumor cells evolve phenotypic adaptations to the toxic effects of acidosis including, for example, increased H^+ transport against concentration gradients across the cell membrane and mutations in acid-induced apoptotic pathways. Normal tissue, lacking these adaptive traits, is vulnerable to acid-mediated toxicity including cell necrosis and apoptosis, and degradation of the extracellular matrix by acid-induces release of cathepsin B and other proteolytic enzymes.

This proposed mechanism of tumor invasion is initially evaluated through mathematical models. Because the tumor-host interface is a highly complex structure, mathematical modeling can

provide insights into the governing nonlinear dynamics not obtainable intuitively. These models show the feasibility of acid-mediated tumor invasion and made detailed predictions regarding the cellular and microenvironmental dynamics of the tumor-host interface which could be tested experimentally (Fig. 1).

The *in vivo* experiments presented in this study confirm the modeling predictions that tumors acidify the extracellular space of normal tissue around the tumor edge. This gradient of acidosis seems quite variable in size ranging from 100 to 400 μm in the PC3N/eGFP line and at least a few millimeters in the MCF7/s line. Our observations suggest that this heterogeneity in the acid gradients is likely dependent on variations in vascular density and blood flow. Each blood vessel may act as a H^+ sink depending on flow rate and the acid gradient across the vessel wall. On histologic sections, we found a significantly increased (but highly variable) vascular density in the tumor edge and the normal tissue immediately adjacent to the edge (see Fig. 6, for example). Integrating the interactions of vessel growth, blood
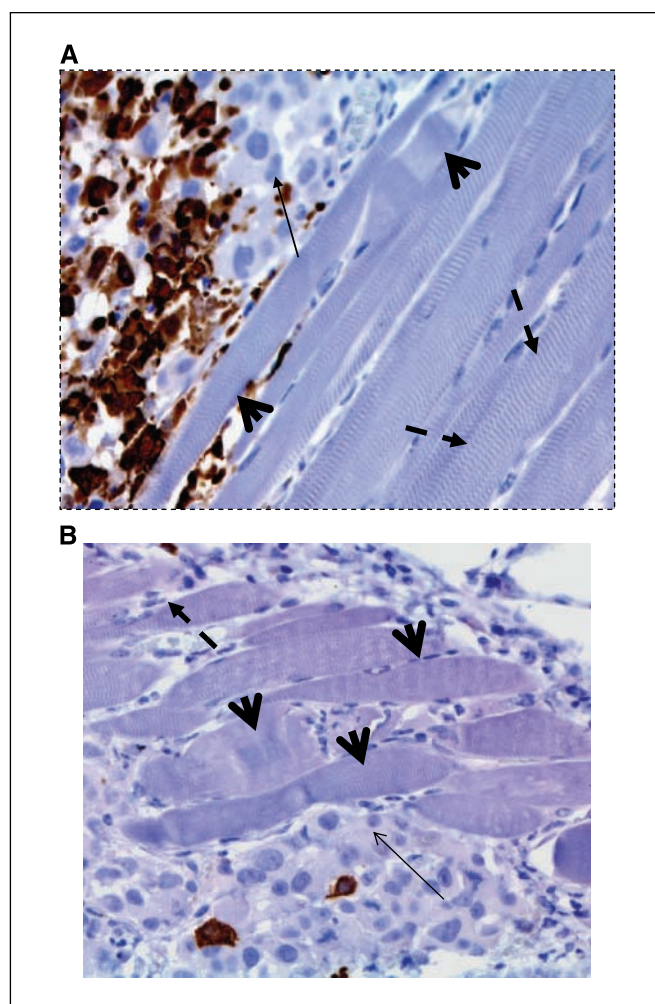

Figure 5. Photomicrographs of the PC3N/eGFP-host interface following H&E and caspase staining. Apoptotic cells are present (*dark area*) are present within and adjacent to the tumor edge (*small arrow*). Skeletal muscle immediately adjacent to the tumor edge (*large arrowheads*) shows evidence of toxicity with loss of normal striation, swelling, and increased eosinophilia. Skeletal muscles more distant from the tumor edge (*dashed arrows*) retain a normal appearance. This generally corresponds to the depth of the pH_e gradient observed on FRIM images.
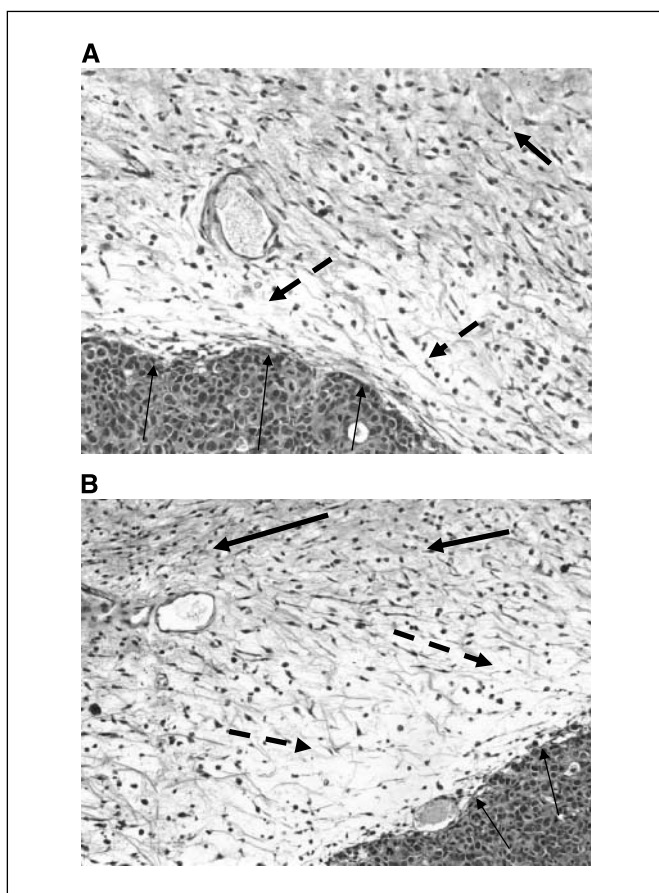
Figure 6. PAS staining of thePC3N/eGFP-host interface regions. There is clear loss of peritumoral extracellular matrix in the immediate region (*dashed arrows*) of the tumor edge (*thin arrows*) roughly corresponding to the acidosis gradient. The more distant extracellular matrix remains more intact (*larger arrows*).

flow, microenvironmental properties, tumor growth, and acid-induced toxicity is a major future goal of this work.

In the PC3N/eGFP line, the peritumoral acid gradient was confined to a region of the chamber and, thus, the potential cellular and extracellular effects of the gradients could be assessed. We did observe evidence of cellular toxicity, apoptosis, and extracellular matrix degradation in the peritumoral normal tissue roughly corresponding to the acid gradient. These findings are consistent with the predictions of the model although limited by their observational and nonquantitative characteristics. Furthermore, we cannot unambiguously determine cause and effect so that it is possible, for example, that the peritumoral pH_e gradient and tissue toxicity may represent manifestations of another underlying process such as increased tumor interstitial pressure. This is particularly the case for observed toxicity in skeletal muscle, which is relatively tolerant of acidic environments (at least over short periods of time). Clearly, additional studies will be required to definitively evaluate the acid-mediated tumor invasion hypothesis.

In conclusion, our multidisciplinary study shows the potential benefits of combining mathematical modeling with experimental studies in the investigation of complex systems dominated by nonlinear dynamics such as the tumor-host interface. Our results show the presence of a peritumoral acid gradient in two xenograft models—confirming a critical prediction of the acid-mediated tumor invasion hypothesis. Our results show evidence of cellular toxicity

and extracellular matrix degradation in this acidic region supporting, but not confirming, the proposal that the gradient plays an important role in promoting tumor invasion. This suggests that continued investigation is warranted both to increase understanding of the critical intracellular and extracellular interactions at the tumor-host interface and develop novel tumor therapy strategies based on perturbations of those system dynamics (23, 36).

Appendix A. Nondimensionalization of the Model

Equations D and E can be nondimensionalized using the following transformations:

$$\eta_1 = N_1/K_1$$

$$\eta_2 = N_2/K_2$$

$$\Lambda = H/H_0 \tag{F}$$

$$\tau = r_1 t$$

$$\xi = \sqrt{r_1/D_N} x$$

which transforms Eqs. D and E into

$$\frac{\partial \eta_1}{\partial \tau} = \eta_1(1 - \eta_1 - \eta_2) - \phi_1(\Lambda)\eta_1 + \nabla_\xi \cdot [(1 - \eta_1 - \eta_2)\nabla_\xi \eta_1]$$

$$\frac{\partial \eta_2}{\partial \tau} = \rho_2 \eta_1(1 - \eta_1 - \eta_2) - \phi_2(\Lambda)\eta_2 + \nabla_\xi \cdot$$
$$[(1 - \eta_1 - \eta_2)\nabla_\xi \eta_2] \tag{G}$$

$$\frac{\partial \Lambda}{\partial \tau} = \rho_3 \eta_2 - \delta_3(\Lambda - 1) + \Delta_3 \nabla_\xi^2 \Lambda$$

where $\rho_2 = r_2/r_1$, $\rho_3 = r_3 K_2/(H_0 r_1)$, $\delta_3 = d_3/r_1$ and $\Delta_3 = D_3/D_N$. The death rate functions are also dimensionless having the form

$$\phi_{1,2}(\Lambda) = \delta_{1,2}\left[1 - \exp\left\{-\left(\frac{\Lambda - \Lambda_{1,2}^{opt}}{2\Lambda_{1,2}^{width}}\right)^2\right\}\right] \tag{H}$$

where $\delta_{1,2} = d_{1,2}/r_1$, $\Lambda_{1,2}^{opt} = H_{1,2}^{opt}/H_0$, and $\Lambda_{1,2}^{width} = H_{1,2}^{width}/H_0$ are all dimensionless as well.

Appendix B. Parameter Estimation

In vitro spheroid doubling times are between 1 and 4 days, therefore, we take $r_2 = \ln 2/2.5$ days $\approx 3.2 \times 10^{-6}$/s. For normal tissue wound healing, 4 days seems reasonable for the doubling time, therefore, we take $r_1 = \ln 2/4.0$ days $\approx 2.0 \times 10^{-6}$/s. We assume that the volume limited carrying capacities of tumor and normal tissue are the same: $K_1 = K_2 \approx 5 \times 10^8$ cells/cm^3.

For vascular evacuation without buffering $d_3 = \alpha p$, where $\alpha \approx$ 200/cm is the vessel areal density and $P \approx 1.2 \times 10^{-4}$ cm/s is the vessel permeability for lactate resulting in a removal rate of 2.4×10^{-2}/s. Local buffering might increase this by 25%, thus, our final estimate for this rate is $d_3 \approx 3.0 \times 10^{-2}$/s.

If we assume the serum $pH_0 = 7.4$ is also the optimal pH for normal tissue growth, we have $H_1^{opt} = H_0 = 3.98 \times 10^{-11}$ mol/cm^3. An optimal pH of 6.8 for tumor growth gives $H_2^{opt} = 1.58 \times 10^{-10}$ mol/cm^3.

The acid production rate is trickier to estimate, therefore, we work backwards from known data. Assuming that we have a tumor sufficiently large that the temporal and spatial derivatives at its core are small. From Eq. E, we see that $r_3 \approx d_3 (H_{core} - H_0) / K_2$. Assuming a core pH of 6.4, we get $r_3 \approx 2.2 \times 10^{-20}$ mol/cell s.[5]

The lactic acid and cellular diffusion constants are, respectively, $D_3 \approx 5 \times 10^{-6}$ cm^2/s and $D_N \approx 2 \times 10^{-10}$ cm^2/s.

The dimensionless variables are, using the above values, as follows:

$\rho_2 = r_2/r_1$	1.6
$\rho_3 = r_3 K_2/(H_0 r_1)$	1.4×10^5
$\delta_3 = d_3/r_1$	1.5×10^4
$\Delta_3 = D_3/D_N$	2.5×10^4
$\Lambda_1^{opt} = H_1^{opt}/H_0$	1.0
$\Lambda_2^{opt} = H_2^{opt}/H_0$	4.0
$\Lambda_1^{width} = H_1^{width}/H_0$	0.1
$\Lambda_2^{width} = H_2^{width}/H_0$	0.4
$\delta_1 = d_1/r_1$	2.0
$\delta_2 = d_2/r_1$	2.0

A plot of the equation versus Λ using the last six variables is shown in the following figure:
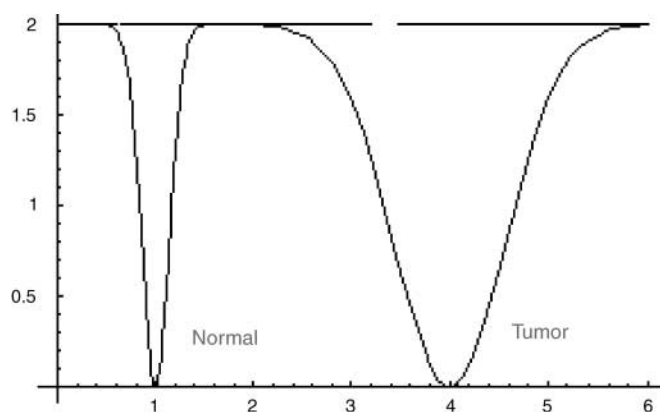
Appendix C. Fixed Points

The fixed points of the model and their stability must be determined numerically. To find the fixed points, we use the acid equation to eliminate Λ from the cellular equations (i.e., the first two in equations with the derivatives set to zero). This leaves two nonlinear equations in two unknowns, i.e., η_1 and η_2. Fortunately, we know that these are physically bounded on the interval (0,1). Therefore, we partition the domain $(0 \leq \eta_1 \leq 1) \otimes (0 \leq \eta_2 \leq 1)$ into a fine rectangular grid with $\Delta\eta_1 = \Delta\eta_2 = 0.01$ and use the grid positions as starting points for a multidimensional Newton-Raphson algorithm. The value of Λ corresponding to a Newton-Raphson solution for the cellular densities is found using the third equation. We save the unique solutions (i.e., those that do not differ from others as determined by the condition $|\eta_{(i)} - \eta_{(j)}| \leq \varepsilon$, with the components of η being η_1 and η_2, and $\varepsilon = 1 \times 10^{-3}$) and determine their stability by numerically computing the eigenvalues of the full three-dimensional Jacobian.

The fixed point analysis for the variables given in the table above is:

```
                Normal:    Tumor:      Acid:
Root 1 found at (0.00000000, 0.00000000, 1.00000000), norm = 0.00000000
UNSTABLE (-1.500000e+04, 1.000000e+00, -4.000000e-01).

Root 2 found at (0.00000000, 0.37206032, 4.47256298), norm = 0.00000000
STABLE (-1.498978e+04, -1.081070e+01, -1.372060e+00).

Root 3 found at (0.00000000, 0.26431209, 3.46691282), norm = 0.00000000
UNSTABLE (-1.500676e+04, 6.337857e+00, -1.264312e+00).

Root 4 found at (0.00000000, -0.25000000, -1.33333333), norm = 0.00000000
UNSTABLE (-1.500000e+04, -7.500000e-01, 4.000000e-01).

Root 5 found at (-0.23499366, -0.01500634, 0.85994078), norm = 0.00000000
UNSTABLE (-1.500000e+04, 1.295203e-01, 1.295203e-01).

Root 6 found at (-0.26500634, 0.01500634, 1.14005922), norm = 0.00000000
UNSTABLE (-1.500000e+04, 1.205189e-01, 1.205189e-01).

Root 7 found at (1.00000000, 0.00000000, 1.00000000), norm = 0.00000000
STABLE (-1.500000e+04, -2.000000e+00, -1.000000e+00).
```

Fixed point no. 1 is trivial and nos. 4, 5, and 6 are nonphysical. Fixed point no. 2 has the tumor beating the normal, however, it is unstable. That leaves fixed points no. 2 and no. 7: although both are stable, the tumor will propagate into the normal because it is in some sense "more stable" (note the relative magnitudes of the corresponding eigenvalues).

Appendix D. Dynamic Simulation

We have developed a method-of-lines parabolic solver that can be used to solve equations subject to the fixed point boundary conditions determined as described above. Initial conditions are taken to be step functions that connect the left and right fixed point boundary conditions.

The following is a typical screen output produced by the solver. <c1>, <c2>, and <c3> are the velocities of the normal, tumor, and acid wavefronts.

```
Advancing solution from   0.00 to  40.00 ... <c1> = 0.294, <c2> = 0.184, <c3> = 0.184
Advancing solution from  40.00 to  80.00 ... <c1> = 0.231, <c2> = 0.226, <c3> = 0.226
Advancing solution from  80.00 to 120.00 ... <c1> = 0.218, <c2> = 0.226, <c3> = 0.226
Advancing solution from 120.00 to 160.00 ... <c1> = 0.226, <c2> = 0.225, <c3> = 0.226
Advancing solution from 160.00 to 200.00 ... <c1> = 0.234, <c2> = 0.226, <c3> = 0.226
Advancing solution from 200.00 to 240.00 ... <c1> = 0.229, <c2> = 0.227, <c3> = 0.226
Advancing solution from 240.00 to 280.00 ... <c1> = 0.216, <c2> = 0.226, <c3> = 0.226
Advancing solution from 280.00 to 320.00 ... <c1> = 0.226, <c2> = 0.225, <c3> = 0.226
Advancing solution from 320.00 to 360.00 ... <c1> = 0.225, <c2> = 0.225, <c3> = 0.226
Advancing solution from 360.00 to 400.00 ... <c1> = 0.216, <c2> = 0.229, <c3> = 0.226
Advancing solution from 400.00 to 440.00 ... <c1> = 0.236, <c2> = 0.226, <c3> = 0.226
Advancing solution from 440.00 to 480.00 ... <c1> = 0.226, <c2> = 0.223, <c3> = 0.226
Advancing solution from 480.00 to 520.00 ... <c1> = 0.225, <c2> = 0.228, <c3> = 0.226
Advancing solution from 520.00 to 560.00 ... <c1> = 0.228, <c2> = 0.229, <c3> = 0.226
Advancing solution from 560.00 to 600.00 ... <c1> = 0.206, <c2> = 0.226, <c3> = 0.226
```

---

[5] This value is remarkably consistent with the curve fit results of the Martin and Jain (34) data to our original, more simplistic model (20).

The wavefront velocities are in dimensionless form and must be multiplied by the velocity scale factor $\sqrt{r_1 D_N}$.

In Fig. 1, we show the profiles after 600 time steps. Notice the interesting features on the tumor and acid edges which correspond to the point in space at which the acid level is optimal for the tumor.

References

1. Gambhir SS. Molecular imaging of cancer with positron emission tomography. Nat Rev Cancer 2002;2:683–93.
2. Rohren EM, Turkington TG, Coleman RE. Clinical application of PET in oncology. Radiology 2004;231:305–32.
3. Mavi A, Lakhani P, Zhuang H, Gupta NC, Alavi A. PET in characterizing solitary pulmonary nodules, assessing pleural diseases, and the initial staging, restaging, therapy planning, and monitoring response of lung cancer. Radiol Clin North Am 2005;43:1–21.
4. Yasuda S, Fujii H, Nakahara T, et al. 18F-FDG PET detection of colonic adenomas. J Nucl Med 2001;42:989–92.
5. Abbey CK, Borowsky AD, McGoldrick ET, et al. *In vivo* PET imaging of progression of transformation in a mouse model of mammary neoplasia. Proc Natl Acad Sci U S A 2004;101:11438–43.
6. Schwarzbach MH, Hinz U, Dimitrakopoulou-Strauss A, et al. Prognostic significance of preoperative [18-F]fluorodeoxyglucose (FDG) positron emission tomography (PET) imaging in patients with resectable soft tissue sarcomas. Ann Surg 2005;241:286–94.
7. Schwartz DL, Rajendran J, Yueh B, et al. FDG-PET prediction of head and neck squamous cell cancer outcomes. Arch Otolaryngol Head Neck Surg 2004;130:1361–5.
8. Vansteenkiste J, Fischer BM, Dooms C, Mortense N. Positron-emission tomography in prognostic and therapeutic assessment of lung cancer: systematic review. Lancet Oncol 2004;5:531–40.
9. Vaupel P, Kallinowski F, Okunieff P. Blood flow, oxygen and nutrient supply, and metabolic microenvironment of human tumors: a review. Cancer Res 1989;49:6449–65.
10. Hatanaka MA. Transport of sugars in tumor cell membranes. Biochim Biophys Acta 1974;335:77–104.
11. Dewhirst MW, Ong ET, Rosner GL, et al. Microvascular studies on the origins of perfusion-limited hypoxia. Br J Cancer 1996;247:51.
12. Kimura H, Braun RD, Ong ET, et al. Fluctuations in red cell flux in tumor microvessels can lead to transient hypoxia and reoxygenation in tumor parenchyma. Cancer Res 1996;56:5522–8.
13. Warburg O. The metabolism of tumors. London: Constable Press; 1930.
14. Lu H, Forbes RA, Verma A. Hypoxia-inducible factor 1 activation by aerobic glycolysis implicates the Warburg effect in carcinogenesis. J Biol Chem 2002;277:23111–5.
15. Gatenby RA. The potential role of transformation-induced metabolic changes in tumor-host interaction. Cancer Res 1995;55:4151–6.
16. Gatenby RA, Gawlinski ET. A reaction-diffusion model of acid-mediated invasion of normal tissue by neoplastic tissue. Cancer Res 1996;56:5745–53.
17. Gatenby RA, Gillies RJ. Why do malignant cancers have high levels of glycolysis? Nat Rev Cancer 2004;4:891–9.
18. Gilead A, Neeman M. Dynamic remodeling of the vascular bed precedes tumor growth: MLS ovarian carcinoma spheroids implanted in nude mice. Neoplasia 1999;1:226–30.
19. Williams AC, Collard TJ, Paraskeva C. An acidic environment leads to p53 dependent induction of apoptosis. Oncogene 1999;16:3199–204.
20. Park HJ, Lyons JC, Ohtsubo T, Song CW. Acidic environment causes apoptosis by increasing caspase activity. Br J Cancer 1999;80:1892–7.
21. Izuishi K, Kato K, Ogura T, Kinoshita T, Esumi H. Remarkable tolerance of tumor cells to nutrient deprivation: possible new biochemical targets for cancer therapy. Cancer Res 2000;60:6201–6.
22. Graeber TG, Osmanian C, Jacks T, et al. Hypoxia-mediated selection of cells with diminished apoptotic potential in solid tumours. Nature 1996;379:88–91.
23. Gatenby RA, Gawlinski ET. The glycolytic phenotype in carcinogenesis and tumor invasion—insights through mathematical models. Cancer Res 2003;63:3847–54.
24. Bhujwalla ZM, Artemov D, Ballesteros P, Cerdan S, Gillies RJ, Solaiyappan M. Combined vascular and extracellular pH imaging of solid tumors. NMR Biomed 2002;15:114–9.
25. Helmlinger G, Yuan F, Dellian M, Jain RK. Interstitial pH and pO^2 gradients in solid tumors *in vivo*: high-resolution measurements reveal a lack of correlation. Nat Med 1997;177–82.
26. Schornack PA, Gillies RJ. Contributions of cell metabolism and H^+ diffusion to the acidic pH of tumors. Neoplasia 2003;5:135–45.
27. Shi Q, Le X, Wang B, et al. Regulation of vascular endothelial growth factor expression by acidosis in human cancer cells. Oncogene 2001;20:3751–6.
28. Fukumura D, Xu L, Chen Y, Gohongi T, Seed B, Jain RK. Hypoxia and acidosis independently up-regulate vascular endothelial growth factor transcription in brain tumors *in vivo*. Cancer Res 2001;61:6020–4.
29. Rohzin J, Sameni M, Ziegler G, Sloane BF. Pericellular pH affects distribution and secretion of cathepsin B in malignant cells. Cancer Res 1994;54:6517–25.
30. Glunde K, Guggino SE, Solaiyappan M, Pathak AP, Ichikawa Y, Bhujwalla ZM. Extracellular acidification alters lysosomal trafficking in human breast cancer cells. Neoplasia 2003;5:533–45.
31. Lardner A. The effects of extracellular pH on immune function. J Leukoc Biol 2001;69:522–30.
32. Dairkee SH, Deng SH, Stampfer MR, Waldman RM, Smith HS. Selective cell culture of primary breast cancer. Cancer Res 1995;55:2516–9.
33. Papenfuss HD, Gross JF, Intaglietta M, Treese FA. A transparent access chamber for the rat dorsal skin fold. Microvasc Res 1979;18:311–8.
34. Martin GR, Jain RK. Noninvasive measurement of interstitial pH profiles in normal and neoplastic tissue using fluorescent ratio imaging microscopy. Cancer Res 1999;54:5670–4.
35. Gillies R, Liu Z, Bhujwalla ZM. ^{31}P-MRS measurements of extracellular pH of tumors using 3-aminopropylphosphonate. Am J Physiol 1994;267:195–203.
36. Gatenby RA, Gawlinski ET, Tangen C, Flanigan RC. The possible role of post-operative azotemia in enhanced survival of patients with metastatic renal cancer following cytoreductive nephrectomy. Cancer Res 2002;62:5218–22.